JME

Journal of Mining & Environment,
Vol.9, No.2, 2018, 513-525.
DOI: 10.22044/jme.2018.6386.1458

Porosity classification from thin sections using image analysis and neural networks including shallow and deep learning in Jahrum formation

M. Abedini[1*], M. Ziaii[1], Y. Negahdarzadeh[1] and J. Ghiasi-Freez[2]

1. Faculty of Mining, Petroleum & Geophysics Engineering, Shahrood University of Technology, Shahrood, Iran
2. Iranian Central Oil Fields Company (ICOFC), Subsidiary of National Iranian Oil Company (NIOC), Iran

Received 2 November 2017; received in revised form 23 January 2018; accepted 26 January 2018
**Corresponding author: abedini.m1992@gmail.com (M. Abedini).*

Abstract
The porosity within a reservoir rock is a basic parameter for the reservoir characterization. The present paper introduces two intelligent models for identification of the porosity types using image analysis. For this aim, firstly, thirteen geometrical parameters of pores of each image were extracted using the image analysis techniques. The extracted features and their corresponding pore types of 682 pores were used for training two intelligent models, BPN (back-propagation network) and SAE (stacked autoencoder). The trained models take the geometrical properties of pores to classify the type of six porosity types including intra-particle, inter-particle, vuggy, moldic, biomoldic, and fracture. The MSE values for the BPN and SAE models were found to be 0.0042 and 0.0038, respectively. The precision, recall, and accuracy of the intelligent models for classifying the types of pores were calculated. The BPN model was able to correctly recognize 193 intra-particle pores out of 197 ones, 45 inter-particle pores out of 50 ones, 7 vuggy pores out of 9 ones, 10 moldic pores out of 12 ones, 2 biomoldic pores out of 3 ones, and 6 fractures out of 7 ones. Also the SAE model was able to correctly classify 193 intra-particle pores out of 197 ones, 46 inter-particle pores out of 50 ones, 8 vuggy pores out of 9 ones, 10 moldic pores out of 12 ones, 3 biomoldic pores out of 3 ones, and 7 fractures out of 7 ones. The results obtained showed that the SAE model carried out a bit more accuracy for classification of the inter-particle, vuggy, biomoldic, and fracture pores.

Keywords: *Porosity Classification, Image Analysis, Neural Network, Deep Learning, Stacked Autoencoder.*

1. Introduction

Porosity is an important parameter of each reservoir rock. Indicating the space available for storage of fluid and a measure of the void spaces in a material, it is defined as a fraction of the volume of voids over the total volume between 0 and 1 or as a percentage between 0 and 100%. There are several types of porosity in the structure of reservoir rocks, each of which playing a different role in flow features of the rocks. Porosity classification is a fundamental procedure from a geological viewpoint. The results of porosity classification can be employed to improve the modeling of reservoir conditions. Studying the thin sections has been one of the popular methods for classification of the porosity types in a rock. It is a time-consuming procedure for expert geologists to characterize each type of porosity in a thin section.

In the last decade, many advances in image analysis, intelligent systems, and pattern recognition techniques have been made in different branches of scientific fields due to their accurate results and rapid measurements. To date, several researchers have worked on the capabilities of thin section images for rock characterization. Also many researchers have focused on the integration of image analysis techniques and intelligent systems by development of intelligent systems, especially neural networks.

Lucia (1983) has proposed a classification of carbonate porosity based on the data derived from visual description. This classification can be used in a field or for a routine laboratory description. Inter-particle porosity was classified according to the particle size and the dense or porous appearance of the inter-particle area. Vuggy porosity was classified according to the type of inter-connection. Separate vugs were connected through inter-particle pore spaces and classified by percent porosity, and touching vugs were connected to each other and classified by presence or absence [1].

Ehrlich et al. (1984) have worked on the analysis of reservoir pore complexes. There is a need to relate the petrology of reservoirs such as pore geometry to the petro-physical data. They developed a petrographic image analysis from the beginning to interface with the petro-physical data. Petrographic image analysis contains hardware and software that carry out four functions including image acquisition, image digitization, image segmentation, and image analysis. They generated separate spectra related to pore size and pore roughness from each image. In addition, surface area per unit volume of pores could be assessed [2].

Funk et al. (1989) have described pore size distributions using petro-physical properties and image analysis. They developed statistical relationships with image analysis techniques, which provided worth information for investigating anomalies in petro-physical properties [3].

Mohaghegh and Ameri (1995) have discussed the importance of artificial neural networks (ANNs) to petroleum engineers and the advantages that this computing process has over other conventional methods and the mechanics by which neural networks achieve their objective. They expressed that ANNs could help petroleum engineers in solving some fundamental petroleum engineering problems. The aim of their work was to encourage engineers and researchers to consider it as a valuable tool in petroleum industry [4].

Van den Berg et al. (2002) have presented an alternative computer algorithm to separate touching grain sections in binary images of granular material. The algorithm detected characteristic sharp contact wedges in the outline of touching grain sections and created an inter-section after checking if the angle of the contact wedge was smaller than a threshold value. The result of grain-size distributions after applying automated separation techniques verified with the size distribution obtained with a laboratory laser particle sizer. The algorithm improved preservation of size and shape characteristics of the granular material [5].

Perring et al. (2004) have used automated digital image analysis to acquire quantitative petrographic data for igneous rocks. This method is not restricted to the study of igneous rocks [6].

Marmo et al. (2005) have proposed a numerical methodology based on the digitized image of thin sections to identify carbonate textures unaffected by post-depositional modifications. The methodology uses, as input, 256 grey-tone digital image, and by image processing gives, as output, a set of 23 values of numerical features measured on the whole image. A multi-layer neural network takes as input these features, and gives, as output, the estimated class. This technique showed 93.3% and 93.5% of accuracy to classify textures of carbonate rocks using digitized images on two test sets, respectively [7].

Al-Bazzaz and al-Mehanna (2007) have used 2D images of thin section and SEM to characterize the morphology of grains and pores for porosity, permeability, and means hydraulic radius calculations [8].

Martinez-Martinez et al. (2007) have demonstrated the efficiency of image analysis as a suitable tool for petrographic quantification of brecciated rock [9].

Dong et al. (2007) have performed analysis of pore size distribution of Arabian core samples. They used X-ray micro-tomography to image rock cuttings. The largest inscribed spheres in the pore space represent pores with throats representing the connections between them. They validated the result through comparison with networks derived by a different method from idealized sphere packing. The goal of their work was to input the models into pore-scale network models to predict macroscopic features. Pore spectra were decomposed and classified using pattern recognition and classification algorithms or used directly to assess physical parameters [10].

Grove and Jerram (2011) have developed an effective method to measure the total optical porosity of impregnated thin sections. The objective of the study included the search for developing a semi-automated model for identification and classification of five types of porosity in thin section images. A semi-automate algorithm was described, which combined the advantages of image analysis and discriminant classifiers to extract the features of pores from the images and categorize them in one of the five

classes, namely inter-particle, intra-particle, oomoldic, biomoldic, and vuggy [11].
Enbaia and Ramdzani (2014) have revised the limitation of pore geometry SEM measurements applied to both the synthetized and real formation samples with the usage of fundamental concepts and available data of pores. They used the digital image analysis to enhance the pore system interpretation. They discussed the concepts like pore throat, body and connectivity, and 2D and 3D analyses to make the actual information of pore geometry that was more useful in drilling and completion design [12].
Suhaimi (2016) has characterized the distribution of pore geometry utilizing the available core data, thin section petrographic image analysis, mercury injection, capillary pressure, and a newly developed depositional model. Three pore types including inter-particle (inter-crystalline), separate vugs, and touching vugs were presented [13].
Recently, deep learning as a branch of neural networks has become one of the favorite methods for the researchers in different cases [14, 15].
Bengio et al. (2007) have originally proposed stacking of autoencoders in order to boost performance of deep networks [16].
Baldi (2012) has presented a general mathematical framework to study both the linear and non-linear autoencoders. The framework allowed to derive an analytical treatment for the most non-linear auto-encoder, the Boolean autoencoder. Learning in the Boolean autoencoder is equivalent to a clustering problem that can be solved when the number of clusters is small and becomes NP complete when the number of cluster is large. **NP** is a complexity class used to describe certain types of decision problems. Informally, **NP** is the set of all decision problems for which the instances where the answer is "yes" have efficiently verifiable proofs [17].
Chen et al. (2014) have introduced the concept of deep learning. First, they verified the eligibility of stacked autoencoders by following spectral information-based classification. Secondly, a new way of classifying with spatial-dominated information was proposed. Then they proposed a novel deep learning framework to merge the two features that could obtain the highest accuracy of classification. Experimental results indicated that classification built in this deep learning-based framework provided competitive performance [18].
Schmidhuber (2015) has reviewed deep supervised learning, unsupervised learning, and indirect search for short programs encoding deep and large networks. Shallow and deep learners are distinguished by the depth of their credit assignment paths, which are chains of possibly learnable, causal links between actions and effects [19].
The proposed methodology in this paper is integration of image analysis and intelligent systems including shallow and deep learning of neural networks.

2. Geology of Jahrum formation

Several thousand meters of carbonate sediments were deposited in the Zagros basin. The Jahrum Formation is located in the Shiraz area. This formation has been assigned to the middle Eocene to Pliocene (Figure 1).
The Jahrum Formation consists of 468 m of dolomite and dolomitic limestone, which are overlain with unconformable and erosional contact by the Asmari Formation [20]. Beneath the Jahrum Formation are the evaporites of the Sachun Formation [21]. This formation mainly consists of dolomite and limestone. In this study, the thin sections of core data of Jahrum Formation were available.

3. Material and methods

3.1. Image analysis

Image analysis is defined as different computer-based levels for identification, description, and diagnosis of the elements from an image. The levels of image analysis for identification of pore spaces include image acquisition, image filtering, image segmentation, and feature extraction.
Image acquisition includes preparing the images from thin sections. A digital camera attached to an optical microscope was used to capture images of thin sections. Field of view is a significant factor of image analysis, and is selected based on visible pores.
The second step of image analysis is image filtering. Inappropriate mounting of slides, uneven thickness of the section, and dirt on the thin section can adversely affect the quality of images [22]. The quality of images affect the performance of feature extraction algorithm.
The image segmentation includes identification and isolation of the pixels that belong to the same class, which can be used for creating a representation of image to detect the important elements for a research work [9]. The image segmentation should be done for separating the pores from the rest of a thin section image. In the RGB model, the red, green, and blue colors are combined to create a wide range of colors. The

model assigns the intensity level of red, green, and blue on a scale of 0 to 255, where 255 represents the maximum intensity. The segmented images will be used for extracting the geometrical parameters. Specifying incorrect definition of pores will cause inaccuracy in the type of porosity.

The last step of image analysis is feature extraction. The accuracy of image analysis depends on the extracted features. The accurate extraction of features authenticates the precision of methodology. Feature extraction defines the significant characteristic of images. The extracted features ought to be signalizing different pores.

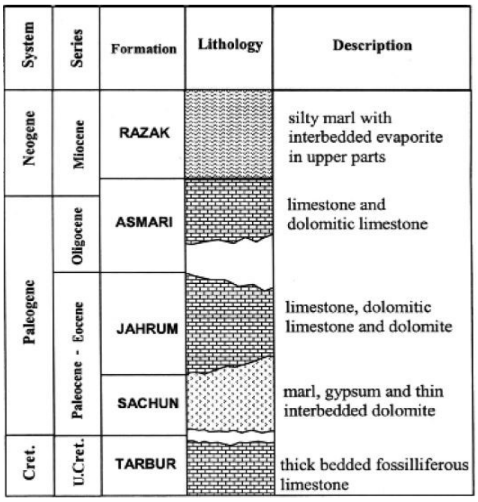

Figure 1. General stratigraphic column for Tertiary interval in Shiraz area [20].

3.2. Artificial neural networks (intelligent systems)

The main purpose of this work was to develop an intelligent model using the training data. There are several types of intelligent systems. Each of them has a set of parameters that are required to be optimized. Shallow and deep learning of neural networks were employed to develop two intelligent models for classifying pore spaces of reservoir rocks.

3.2.1. Shallow learning of neural network

The structure of a feed-forward neural network is mentioned in Figure 2. A feed-forward neural network often has one hidden layer of sigmoid neurons and an output layer of linear neurons. The neurons with non-linear transfer functions permit the network to learn non-linear relationships between input and output [23]. This neural network was trained with a back-propagation learning algorithm [24]. A back-propagation neural network (BPN) is a supervised learning method. BPN computes the difference between the calculated output and corresponding desired output from the training data. Then the error propagated backward through the network and the weights are adjusted during a number of iterations. The training stops when the best approximations of desired values are calculated [25].

3.2.2. Deep learning (SAE) of neural network

Deep learning also known as deep structured learning, hierarchical learning or deep machine learning is a branch of machine-learning based on learning representations of data. An observation, for example an image, can be represented in many ways such as a vector of intensity values. The sub-categories of deep learning method is described in Figure 3.

In a simple case, you could have two sets of neurons: the ones that receive an input and the ones that send an output. When the input layer receives an input, it passes on a modified version of the input to the next layer. In a deep network, there are many layers between the input and output, and the layers are not made of neurons allowing the algorithm to use multiple processing layers composed of multiple linear and non-linear transformations [19, 26-32].

There are a huge number of various deep learning architectures such as autoencoders. They have been applied to fields like computer vision. Most of them are branched from some original parent architectures. It is not always possible to compare the performance of multiple architectures all together because they are not all evaluated on the same datasets. A research work in this area attempts to construct better representations and create models to learn these representations from large-scale unlabeled data. Some of the representations are inspired by advances in neuroscience, and are loosely based on interpretation of information processing and communication patterns in a nervous system such as neural coding, which attempts to define a relationship between various stimuli and associated neuronal responses in the brain [33].

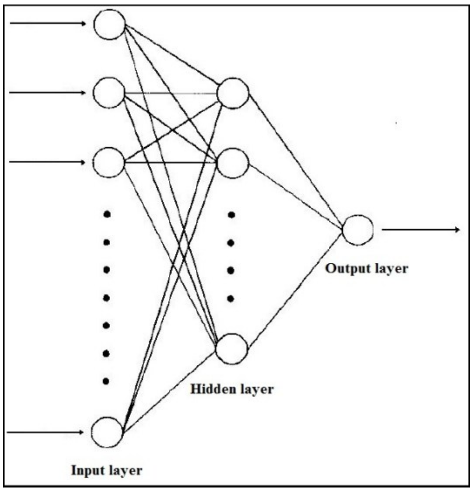

Figure 2. Structure of a feed-forward neural network [24].

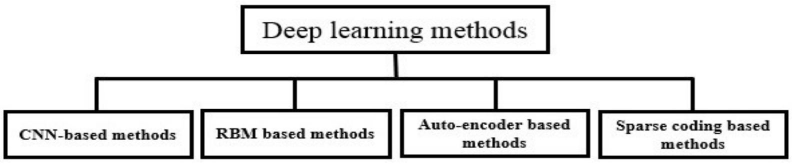

Figure 3. Sub-categories of deep learning method.

3.2.2.1. Autoencoders

A single autoencoder is a two-layer neural network used for unsupervised deep learning of efficient coding [34, 35]. The target of an autoencoder is to learn a representation for a set of data, typically for the purpose of dimensionality reduction [36]. An autoencoder consists of an encoder layer and a decoder layer. The encoder layer maps the input to a hidden representation. The decoder layer attempts to map this representation back to the original input [23]. In other word, the encoding layer encodes the inputs of the network, and the decoding layer decodes the inputs. As a result, the number of neurons in the encoding layer is equal to the input dimensionality [37]. An autoencoder applies back-propagation. An autoencoder is shown in Figure 4.

The autoencoder attempts to learn a function, $h_{W,b}(X) \approx X$. In other words, it tries to learn an approximation to the identify function so as to output $\hat{X}$ that is similar to X [38]. In other words, the target of an autoencoder is to compute a code h of an input instance x from which x can be recovered with high accuracy [37].

3.2.2.2. Stacked autoencoders

Stacked autoencoder is unsupervised pre-training, layer by layer, as input is fed through. Once, the first layer is pre-trained, it can be used as an input of the next autoencoder. Therefore, an autoencoder on the row input x_k is trained to learn primary features $h_k^{(1)}$ (Figure 5A). Next, these primary features are used as the raw input to another autoencoder to learn the secondary features, $h_k^{(2)}$ (Figure 5B). Following this, these secondary features are used as a raw input to a softmax layer (Figure 5C). Actually, the final layer can deal with the traditional supervised classification, and the pre-trained neural network can be fine-tuned using back-propagation. The output of softmax node is in terms of the probabilities of each class. Therefore, gradients at each node are computed with softmax and cross entropy performance function. Finally, three layers are combined to form a stacked autoencoder with two hidden layers and a final softmax classifier layer (Figure 5D) [38].

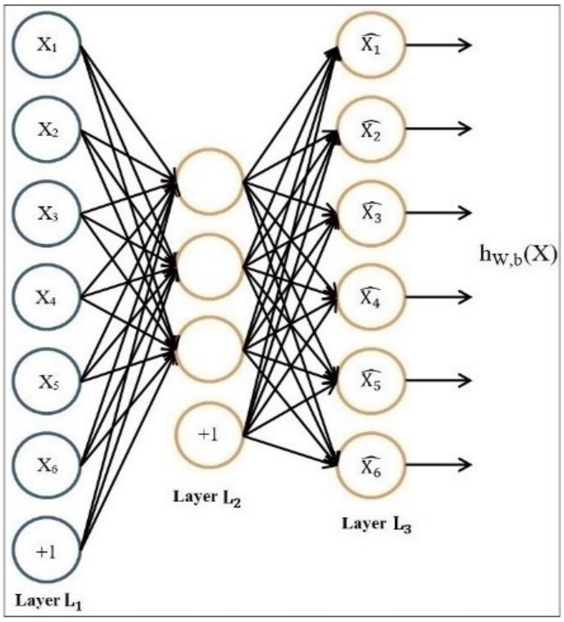

Figure 4. Autoencoder mechanism [38].

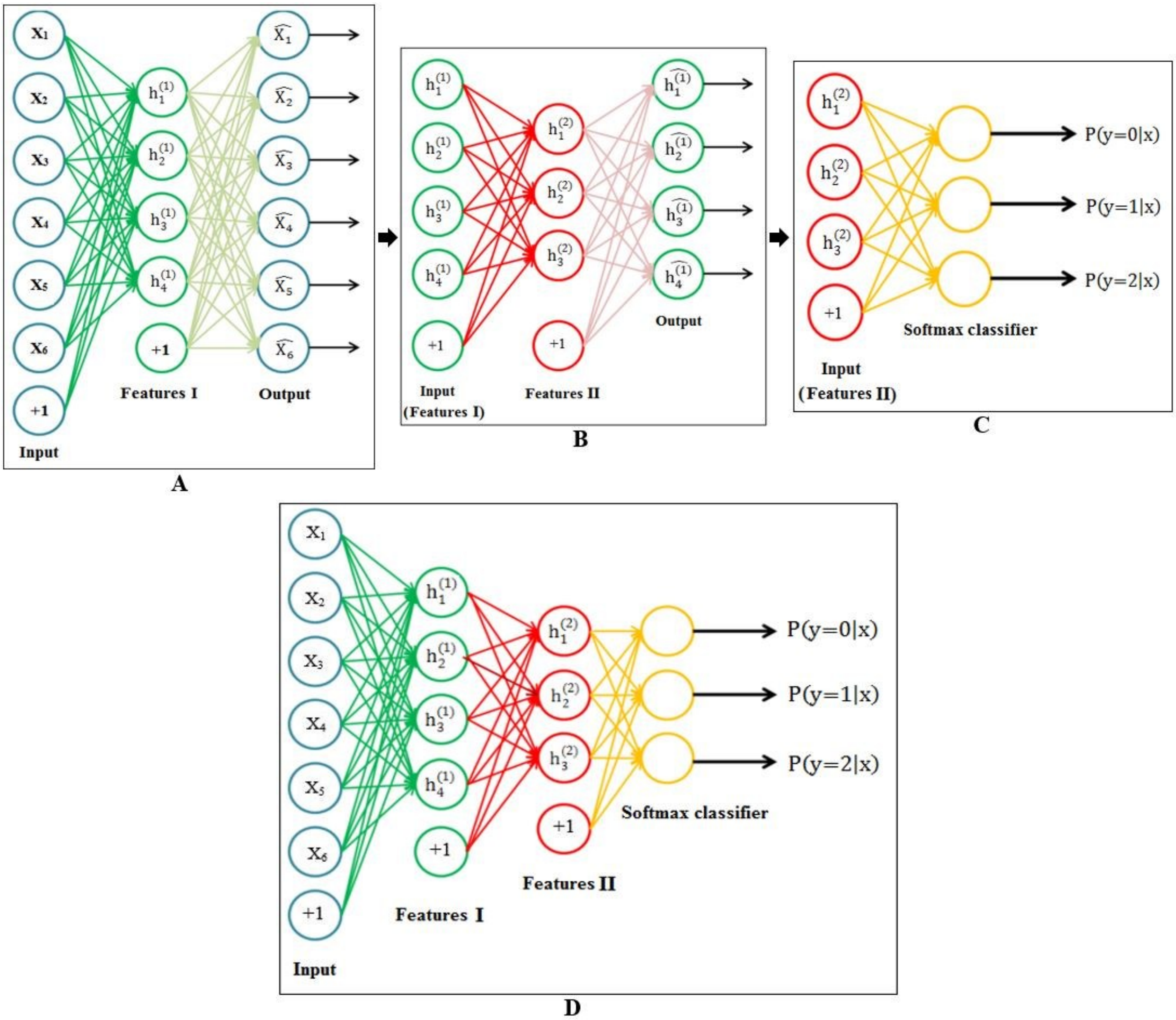

Figure 5. Stacked autoencoder mechanism. Detailed explanation of A, B, C, and D is mentioned in text [38].

4. Calculation

In this section, the benefits of image analysis and intelligent systems were combined while the inputs of intelligent models were prepared through image analysis. In this work, the method introduced by Lonoy (2006) was used to classify the types of porosity [39].

4.1. Data preparation with image analysis

The four steps of image analysis were considered. The images were captured under different fields of view. The trial-and-error examinations demonstrated that the field of view at 40X was suitable. To improve the quality of images and remove the noises from the images, three types of filters including the median, erode, and dilate filters were used. The median filter removes small discontinuities without geometrical changes within pores. The erode and dilate filters erode and enlarge the edges of pores, respectively. In all images, blue pixels were considered as pores because the understudied samples were saturated with blue epoxy. To specify the interval of color intensity for pixels related to the pores, the intensities of red and green colors were below 203 and the intensity of blue color trespassed 170. All pixels with the mentioned red, green, and blue intensities were converted to a unique blue, and the remaining pixels became white. This blue-white image is a 3D one, every pixel including three components of red, green, and blue. The 3D image was converted into a 2D or binary image. Each pixel of a binary image is identified with the zero and one character. In a binary image, pores are shown by black pixels (zero) and other parts of image are defined by white pixels (one) (Figure 6).

Several geometrical features were tested in order to choose the most suitable ones for assessing the size and shape of pores. Finally, the following features were chosen:

Area, area/box, major axis, minor axis, aspect ratio, box (X/Y), mean diameter, mean ferret, IOD, radius ratio, roundness, size (length), size (width) (Table 1).

A graphical description of geometrical properties is demonstrated in Figure 7. The geometrical features of 960 pores were extracted from 59 images of thin sections.

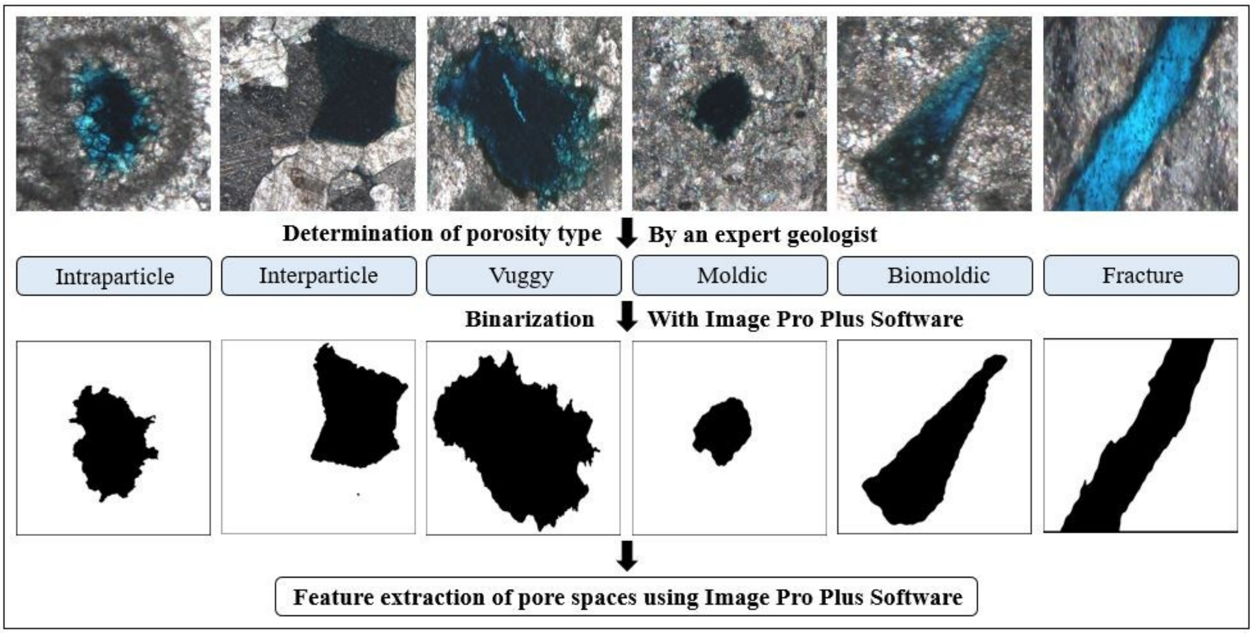

Figure 6. Flowchart of data preparation with image analysis.

Table 1. Definition of selected features.

Marking	Feature	Definition
1	Area	Number of pixel in a pore
2	Area/Box	Ratio between area of pore and area of its bounding box
3	Major axis	Length of major axis of ellipse
4	Minor axis	Length of minor axis of ellipse
5	Aspect ratio	Ratio between major axis and minor axis of ellipse equivalent to object
6	Box (X/Y)	Ratio between width and height of pore's bounding box
7	Mean diameter	Average length of diameters measured at 2 degree intervals and passing through object's centroid
8	Feret (mean)	Average caliper (feret) length
9	IOD	Multiplication of area and average intensity
10	Radius ratio	Ratio between maximum and minimum radius
11	roundness	Ratio of perimeter to area of a pore
12	Size (length)	Feret diameter along major axis of pore
13	Size (width)	Feret diameter along minor axis of pore

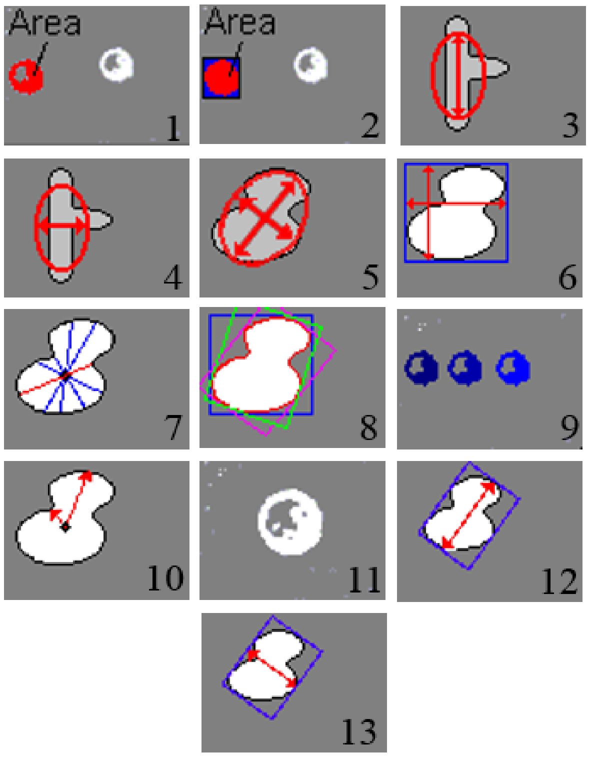

Figure 7. Graphical description of selected geometrical features. 1) Area, 2) Area/Box, 3) Major axis, 4) Minor axis, 5) Aspect ratio, 6) Box (X/Y), 7) Mean diameter, 8) Mean ferret, 9) IOD, 10) Radius ratio, 11) Roundness, 12) Size (length), 13) Size (width).

4.2. Training intelligent systems

The geometrical properties extracted in the image analysis stage were used as inputs of intelligent systems, from which 682 and 278 pores were considered for the training and testing procedures, respectively.

For preparation of the training data, 509 intra-particle, 103 inter-particle, 37 vuggy, 20 moldic, 5 biomoldic porosity, and 8 fracture were investigated. The largest percentage of the training data belonged to the intra-particle pore. Inter-particle pores had the most complex geometrical shapes. Also the testing data included 197 intra-particle, 50 inter-particle, 9 vuggy, 12 moldic, 3 biomoldic porosity, and 7 fracture (Figure 8).

The extracted geometrical features and their corresponding pore types of 682 pores were used for training two intelligent systems, namely BPN and SAE. Intelligent systems along with training save the area of the studied pores in the memory.

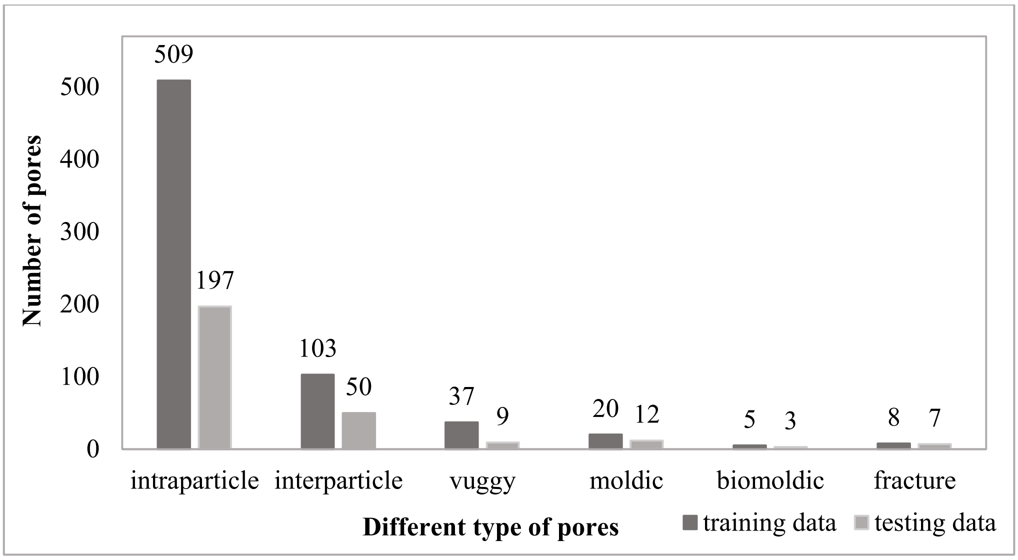

Figure 8. Histograms of distribution of pore types.

4.3. Construction of BPN model (back-propagation network)

The training algorithm was applied for updating the weights and bias values of a three-layered error back-propagation algorithm. The specifications of the created model is mentioned in Table 2. The performance of the BPN model was equal to 0.0057 for the training data.

After training the network, the test data was introduced to the BPN model and the type of porosity was determined. The measured mean squared error (MSE) for the test data was equal to 0.0042.

Table 2. Specifications of BPN model.

Type of network	Feed-forward back-propagation
Training function	TRAINLM
Adaption learning function	LEARNGDM
Performance function	MSE
Number of layers	3
Number of neurons	30
Transfer function between layers	TANSIG

4.4. Construction of SAE model (stacked autoencoder)

The two autoencoders were stacked to construct the SAE model. In the first autoencoder, the hidden layer included 30 neurons, and the PURELIN function was used as the transfer function. In the second autoencoder, the hidden layer included 40 neurons, and the LOGSIG function was employed as the transfer function. With stacking these two autoencoders, the SAE model was created. The characteristics of the constructed model are introduced in Table 3. The performance of the SAE model was equal to 0.0012 for the training data.

After training the network, the test data was introduced to the SAE model, and the type of porosity was determined. MSE for the test data was equal to 0.0038.

Table 3. Characteristics of SAE model.

Type of network	Stacked autoencoder
Training function	TRAINSCG
Performance function	Cross entropy
First autoencoder	
Number of layers	3
Number of neurons	30
Transfer function between layers	PURELIN
Second autoencoder	
Number of layers	3
Number of neurons	40
Transfer function between layers	LOGSIG

4.5. Performance of models

After the training and constructing procedures, an error calculation step was performed to analyze the ability of the intelligent models for new geometrical features that could be introduced as the testing data. The extracted geometrical features of 278 pores were selected for testing the two intelligent systems. The accuracy of the models was calculated. The type of porosity predicted via the intelligent models was compared with the type of porosity determined by an expert geologist.

This investigation provided the final results for classification of each porosity type but did not clarify what accuracy the models had in differentiation of pores individually. The models might predict vuggy porosity as interparticle porosity. Thus it was essential to separately investigate the accuracy of models for classifying the different types of porosity. For this aim, the extracted features of 278 pores including 197 intra-particle, 50 inter-particle, 9 vuggy, 12 moldic, 3 biomoldic porosity, and 7 fracture were used.

Performance of the intelligent models for identifying different pores were compared in Table 4. It was shown that the BPN model correctly identified 193 intra-particle pores out of 197 ones, 45 inter-particle pores out of 50 ones, 7 vuggy porosity out of 9 ones, 10 moldic porosity out of 12 ones, 2 biomoldic porosity out of 3 ones, and 6 fracture out of 7 ones. The SAE model correctly identified 193 intra-particle pores out of 197 ones, 46 inter-particle pores out of 50 ones, 8 vuggy porosity out of 9 ones, 10 moldic porosity out of 12 ones, 3 biomoldic porosity out of 3 ones, and 7 fracture out of 7 ones.

Table 4. Comparison between results of two intelligent models.

Types of porosity	Result of BPN model					
	intra	**inter**	**vuggy**	**moldic**	**biomoldic**	**fracture**
intra	193	4				
inter	5	45				
vuggy		2	7			
moldic	1	1		10		
biomoldic					2	1
fracture					1	6
Precision (%)	96.98	86.54	100	100	66.67	85.71
Recall (%)	97.97	90	77.78	83.33	66.67	85.71
Accuracy (%)	94.60					
Types of porosity	**Result of SAE model**					
	intra	**inter**	**vuggy**	**moldic**	**biomoldic**	**fracture**
intra	193	4				
inter	4	46				
vuggy			8			1
moldic		2		10		
biomoldic					3	
fracture						7
Precision (%)	97.97	88.46	100	100	100	100
Recall (%)	97.97	92	88.89	83.33	100	100
Accuracy (%)	96.04					

5. Results and conclusions

- Porosity classification plays a significant role in the permeability evaluation and reservoir characterization. Therefore, the target of this work was porosity classification using image analysis and intelligent systems. Pore types including intra-particle, inter-particle, vuggy, moldic, and fracture are common and important in carbonate rocks [40]. These porosity types were perused in the studied thin sections.
- The main factors influencing the accuracy of intelligent models are quality, quantity, and type of training data. Various geometrical features of six types of porosity were studied in order to determine the wide range of porosity types. The types of verified porosity were determined by an expert geologist. Then their geometrical features were calculated. According to the objective followed in any pattern recognition study, a suitable kind of input data must be selected.
- For recognizing specific pores within an image, one is required to investigate those features used by human brain to differentiate between pores and other parts. The geometrical properties of pores were applied by human brain for differentiating pores. Therefore, in this work, the advantage of

geometrical properties was used as a tool to differentiate and classify pores.

- It is impossible to precisely classify the types of porosity in thin sections by exclusively using optical investigation and without support of intelligent techniques. Therefore, two suitable models were presented to meet this aim in this work.
- Thirteen geometrical features of pores were extracted from segmented images. Then these features were used as the inputs of two kinds of intelligent systems. The training set of selected pores with different and complex geometrical shapes causes the accurate performance of intelligent models as an applicable tools for classifying six types of pore spaces. Therefore, the developed functions can be confidently used in the future works.
- Deep learning is a fast-growing field. Recently, the autoencoder concept has become more widely used for learning generative models of data [41]. The stacked autoencoder has two facades: a list of autoencoders and a multiple layer perceptron (MLP). During pre-training, the first facade is used, model is treated as a list of autoencoders, and each autoencoder is trained separately. In the second stage of training, the second facade is used. These two facades are linked since the autoencoders and the sigmoid layers of the MLP share parameters and the latent representations computed by intermediate layers of the MLP are fed as input to the autoencoders.
- The models might assess vuggy porosity as inter-particle porosity. Therefore, it is necessary to separately check the accuracy of the models in order to identify different types of pores. Among 278 pores, 197 intra-particle, 50 inter-particle, 9 vuggy, 12 moldic, 3 biomoldic, and 7 fracture were identified. Accuracies of the BPN and SAE models were 0.9460 and 0.9604, respectively. Recall of the two intelligent models for classifying the six types of porosity was compared in Figure 9.

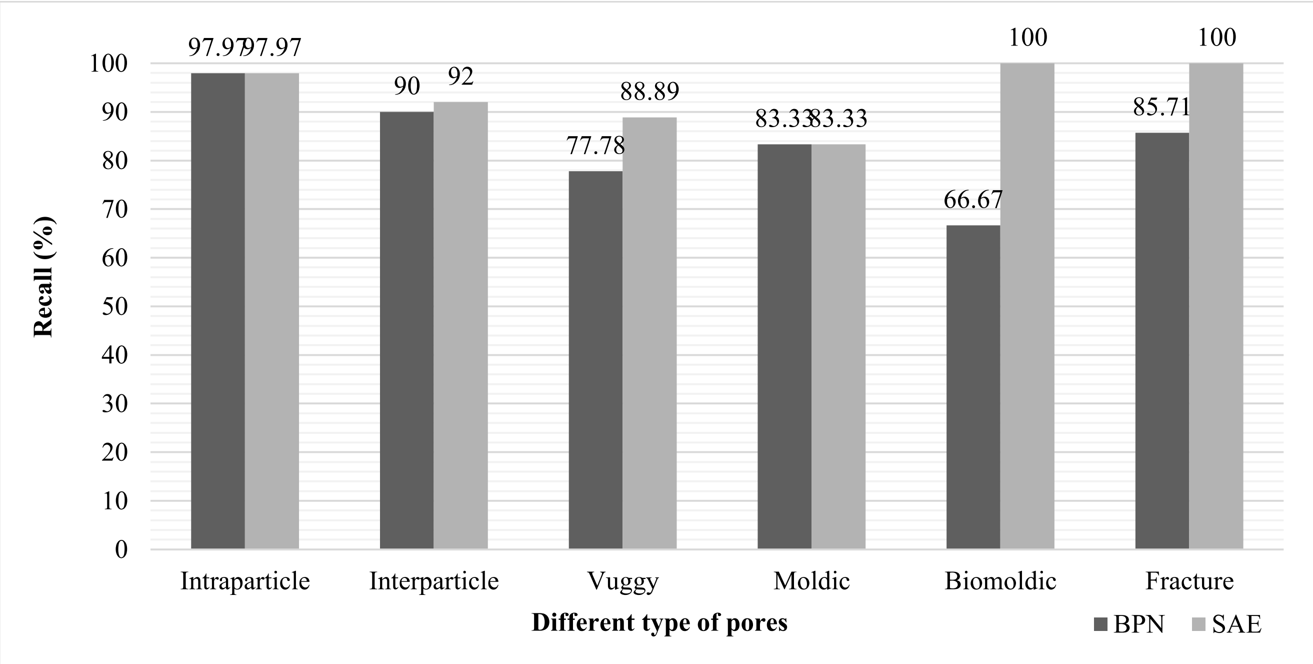

Figure 9. Comparison between Recall of BPN and SAE models for classifying pore types.

- The SAE model carried out a bit more accuracy for identifying the inter-particle, vuggy, biomoldic, and fracture pores. The SAE model performed as accurate as the BPN model for classifying the intra-particle and moldic pores.
- Using image analysis and intelligent systems are useful for porosity classification. Between the two types of intelligent systems including shallow learning (BPN) and deep learning (SAE), the SAE model operates better than the BPN model.
- There is a relationship between porosity and permeability, and therefore, the proposed method in this work can help extraction and investigation of petro-physical features of thin sections as well as permeability prediction.
- It must be mentioned that the model might have restriction in classifying the complicated samples.

Acknowledgments
The authors would like to thank the Shahrood University of Technology for providing the technical supports during this research work.

References
[1]. Lucia, F.J. (1983). Petrophysical parameters estimated from visual descriptions of carbonate rocks: a field classification of carbonate pore space. Journal of Petroleum Technology. 35 (03): 629-637.

[2]. Ehrlich, R., Kennedy, S.K., Crabtree, S.J. and Cannon, R.L. (1984). Petrographic image analysis, I. Analysis of reservoir pore complexes. Sedimentary Research. 54 (4): 1365-1378.

[3]. Funk, J.J., Choinski, M.C., Saxman, B.B. and Callender, C.A. (1989). Characterization of carbonate porosity using petrophysical properties and image analysis. Middle East Oil Show. 11-14 March. Bahrain. pp. 143-153.

[4]. Mohaghegh, S. and Ameri, S. (1995). Artificial neural network as a valuable tool for petroleum engineers, SPE Petroleum Computer Conference. Texas. 29220. pp. 1-6

[5]. Van den Berg, E.H., Meesters, A.G.C.A., Kenter, J.A.M. and Schlager, W. (2002). Automated separation of touching grains in digital images of thin sections. Computers & geosciences. 28 (2): 179-190.

[6]. Perring, C.S., Barnes, S.J., Verrall, M. and Hill, R.E.T. (2004). Using automated digital image analysis to provide quantitative petrographic data on olivine-phyric basalts. Computers & Geosciences. 30 (2): 183-195.

[7]. Marmo, R., Amodio, S., Tagliaferri, R., Ferreri, V. and Longo, G. (2005). Textural identification of carbonate rocks by image processing and neural network: Methodology proposal and examples. Computers & geosciences. 31 (5): 649-659.

[8]. Al-Bazzaz, W.H. and Al-Mehanna, Y. (2007). Porosity, Permeability, and MHR Calculations Using SEM and Thin-section Images for Characterizing Complex Mauddud-Burgan Carbonate Reservoir. Asia Pacific Oil and Gas Conference and Exhibition. 30 October-1 November. Jakarta. Indonesia. pp. 1-9.

[9]. Martinez-Martinez, J., Benavente, D. and Garcı´adel Cura, M.A. (2007). Petrographic quantification of brecciated rocks by image analysis. Application to the interpretation of elastic wave velocities. Journal of Engineering Geology. 90: 41-54.

[10]. Dong, H., Touati, M. and Blunt, M.J. (2007). Pore network modeling: analysis of pore size distribution of Arabian core samples. SPE Middle East Oil and Gas Show and Conference. 11-14 March. Manama. Bahrain. 105156. pp. 1-5.

[11]. Grove, C. and Jerram, D.A. (2011). jPOR: An ImageJ macro to quantify total optical porosity from blue-stained thin sections. Computers & Geosciences. 37 (11): 1850-1859.

[12]. Enbaia, A.E. and Ramdzani, I.A.B.A. (2014). Pore size and geometry of reservoir rocks used as key factor for drilling and completion fluid design of oil wells. European Scientific. 10 (10): 102-113.

[13]. Suhaimi, A.A. (2016). Pore Characterizations and Distributions within Niagaran–Lower Salina Reef Complex Reservoirs in the Silurian Northern Niagaran Pinnacle Reef Trend, Michigan Basin. M.Sc. Thesis. Geoscience department. Western Michigan University. 198 P.

[14]. Hinton, G.E., Osindero, S. and Teh, Y.W. (2006). A fast learning algorithm for deep belief nets. Journal of Neural computation. 18 (7): 1527-1554.

[15]. Deng, L. and Yu, D. (2014). Deep learning: methods and applications. Journal of Foundations and Trends in Signal Processing. 7 (3-4): 198-201.

[16]. Bengio, Y., Lamblin, P., Popovici, D. and Larochelle, H. (2006). Greedy layer-wise training of deep networks. 20th Annual Conference on Neural Information Processing Systems (NIPS 2006). 4-7 December. Vancouver. Canada. pp. 153-160.

[17]. Baldi, P. (2012). Autoencoders, unsupervised learning, and deep architectures. ICML unsupervised and transfer learning. 27 (1): 37-50.

[18]. Chen, Y., Lin, Z., Zhao, X., Wang, G. and Gu, Y. (2014). Deep learning-based classification of hyperspectral data. Selected topics in applied earth observations and remote sensing. 7 (6): 2094-2107.

[19]. Schmidhuber, J. (2015). Deep learning in neural networks: An overview. Neural networks. 61: 85-117.

[20]. Nadjafi, M., Mahboubi, A., Moussavi-Harami, R. and Mirzaee, R. (2004). Depositional history and sequence stratigraphy of outcropping Tertiary carbonates in the Jahrum and Asmari Formations, Shiraz area (SW Iran). Journal of Petroleum Geology. 27 (2): 179-190.

[21]. Motiei, H. (1993). Geology of Iran: Stratigraphy of Zagros. Geological Survey of Iran.

[22]. Rittscher, J., Machiraju, R. and Wong, S. (2008). Microscopic image analysis for life science application. Artech House. Norwood. MA. 489 P.

[23]. Hudson Beale, M., Hagan, M.T. and Demuth, H.B. (2017). Matlab user's Guide: Neural Network Toolbox. Mathwork Inc., Natick. MA. USA. pp. 2-3.

[24]. Svozil, D., Kvasnicka, V. and Pospichal, J. (1997). Introduction to multi-layer feed-forward neural networks. Journal of Chemometrics and intelligent laboratory systems. 39 (1): 43-62.

[25]. Bhatt, A. and Helle, H.B. (2002). Committee neural networks for porosity and permeability

prediction from well logs. Geophysical Prospecting. 50 (6): 645-660.

[26]. Bengio, Y. (2009). Learning deep architectures for AI. Foundations and trends in Machine Learning. 2 (1): 1-127.

[27]. Arel, I., Rose, D.C. and Karnowski, T.P. (2010). Deep machine learning-a new frontier in artificial intelligence research. IEEE Computational Intelligence Magazine. 5 (4): 13-18.

[28]. Bengio, Y., Courville, A. and Vincent, P. (2013). Representation learning: A review and new perspectives. IEEE transactions on pattern analysis and machine intelligence. 35 (8): 1798-1828.

[29]. Deng, L. and Dong, Y. (2014). Foundations and Trends in Signal Processing. Signal Processing. 7: 3-4.

[30]. LeCun, Y., Bengio, Y. and Hinton, G. (2015). Deep learning. Nature. 521 (7553): 436-444.

[31]. Schmidhuber, J. (2015). Deep Learning. Scholarpedia. 10 (11): 32832.

[32]. Goodfellow, I., Bengio, Y. and Courville, A. (2016). Deep learning. MIT Press. Cambridge. MA. 161 P.

[33]. Olshausen, B.A. (1996). Emergence of simple-cell receptive field properties by learning a sparse code for natural images. Nature. 381 (6583): 607-609.

[34]. Liou, C.Y., Huang, J.C. and Yang, W.C. (2008). Modeling word perception using the Elman network. Neurocomputing. 71 (16): 3150-3157.

[35]. Liou, C.Y., Cheng, C.W., Liou, J.W. and Liou, D.R. (2014). Autoencoder for Words. Neurocomputing. 139: 84-96.

[36]. Kingma, D.P. and Welling, M. (2013). Auto-encoding variational bayes. 2nd International Conference on Learning Representations (ICLR). 2-4 May. Scottsdale. Arizona. pp. 1-14.

[37]. Arnold, L., Rebecchi, S., Chevallier, S. and Paugam-Moisy, H. (2011). An introduction to deep learning. 19th European Symposium on Artificial Neural Networks (ESANN 2011). 27-29April. Bruges. Belgium. pp. 477-488.

[38]. Ng, A., Ngiam, J., Foo, C.Y., Mai, Y. and Suen, C. (2010). UFLDL Tutorial: Unsupervised Feature Learning and Deep Learning.

[39]. Lonoy, A. (2006). Making sense of carbonate pore systems. AAPG bulletin. 90 (9): 1381-1405.

[40]. Choquette, P.W. and Pray, L.C. (1970). Geological nomenclature and classification of porosity in sedimentary carbonates. AAPG Bulletin. 54: 207-250.

[41]. Boesen, A., Larsen, L. and Sonderby, S.K. (2015). Generating Faces with Torch.

طبقه‌بندی تخلخل مقاطع نازک با استفاده از آنالیز تصویر و شبکه‌های عصبی با یادگیری کم‌عمق و عمیق در سازند جهرم

مهناز عابدینی[1*]، منصور ضیائی[1]، یاسمن نگهدارزاده[1] و جواد قیاسی فریز[2]

۱- دانشکده مهندسی معدن، نفت و ژئوفیزیک، دانشگاه صنعتی شاهرود، ایران

۲- شرکت نفت مناطق مرکزی ایران، وابسته به شرکت ملی نفت ایران، ایران

ارسال ۲۰۱۷/۱۱/۲، پذیرش ۲۰۱۸/۱/۲۶

* نویسنده مسئول مکاتبات: abedini.m1992@gmail.com

چکیده:

تخلخل سنگ مخزن، پارامتری اساسی برای توصیف سنگ مخزن است. در این پژوهش، برای شناسایی انواع تخلخل، دو مدل هوشمند با استفاده از آنالیز تصویر معرفی می‌شود. بدین منظور، ابتدا سیزده پارامتر هندسی با استفاده از روش آنالیز تصویر از فضاهای خالی در هر تصویر استخراج شد. ویژگی‌های استخراج شده و نوع فضای خالی متناظر، مربوط به ۶۸۲ فضای خالی برای آموزش دو مدل هوشمند پیشرو- پس انتشار خطا (BPN) و خود رمزگذار انباشته (SAE) مورد استفاده قرار گرفتند. مدل‌های آموزش یافته، از ویژگی‌های هندسی فضاهای خالی برای طبقه‌بندی شش نوع تخلخل شامل درون‌دانه‌ای، بین‌دانه‌ای، حفره‌ای، قالبی، بیومولدیک و شکستگی استفاده می‌کنند. میانگین مربعات خطای مدل‌های BPN و SAE به ترتیب ۰/۰۰۴۲ و ۰/۰۰۳۸ محاسبه شد. سپس، معیارهای Precision، Recall و Accuracy مدل‌های هوشمند برای طبقه‌بندی تخلخل محاسبه شد. مدل BPN، ۱۹۳ از ۱۹۷ تخلخل درون‌دانه‌ای، ۴۵ از ۵۰ تخلخل بین‌دانه‌ای، ۷ از ۹ تخلخل حفره‌ای، ۱۰ از ۱۲ تخلخل قالبی، ۲ از ۳ تخلخل بیومولدیک و ۶ از ۷ شکستگی را به درستی شناسایی کرد. همچنین، مدل SAE، ۱۹۳ از ۱۹۷ تخلخل درون‌دانه‌ای، ۴۶ از ۵۰ تخلخل بین‌دانه‌ای، ۸ از ۹ تخلخل حفره‌ای، ۱۰ از ۱۲ تخلخل قالبی، ۳ از ۳ تخلخل بیومولدیک و ۷ از ۷ شکستگی را به درستی طبقه‌بندی کرد. نتایج نشان می‌دهد مدل SAE، دقت بیشتری برای طبقه‌بندی فضاهای خالی بین‌دانه‌ای، حفره‌ای، بیومولدیک و شکستگی داشت.

کلمات کلیدی: طبقه‌بندی تخلخل، آنالیز تصویر، شبکه عصبی، یادگیری عمیق، خود رمزگذار انباشته.
